

Helical superstructures between amyloid and collagen in cardiac fibrils from a patient with AL amyloidosis

Received: 17 November 2023

Accepted: 18 July 2024

Published online: 28 July 2024

 Check for updates

Tim Schulte^{1,2,12}, Antonio Chaves-Sanjuan^{3,12}, Valentina Speranzini^{3,12}, Kevin Sicking^{4,5}, Melissa Milazzo³, Giulia Mazzini⁶, Paola Rognoni⁶, Serena Caminito⁶, Paolo Milani⁶, Chiara Marabelli³, Alessandro Corbelli⁷, Luisa Diomede⁷, Fabio Fiordaliso⁷, Luigi Anastasia^{1,8}, Carlo Pappone^{1,8,9}, Giampaolo Merlini⁶, Martino Bolognesi³, Mario Nuvolone⁶, Rubén Fernández-Busnadiego^{4,5,10,11}, Giovanni Palladini⁶ & Stefano Ricagno^{1,3} ✉

Systemic light chain (LC) amyloidosis (AL) is a disease where organs are damaged by an overload of a misfolded patient-specific antibody-derived LC, secreted by an abnormal B cell clone. The high LC concentration in the blood leads to amyloid deposition at organ sites. Indeed, cryogenic electron microscopy (cryo-EM) has revealed unique amyloid folds for heart-derived fibrils taken from different patients. Here, we present the cryo-EM structure of heart-derived AL amyloid (AL59) from another patient with severe cardiac involvement. The double-layered structure displays a u-shaped core that is closed by a β -arc lid and extended by a straight tail. Noteworthy, the fibril harbours an extended constant domain fragment, thus ruling out the variable domain as sole amyloid building block. Surprisingly, the fibrils were abundantly concatenated with a proteinaceous polymer, here identified as collagen VI (COLVI) by immuno-electron microscopy (IEM) and mass-spectrometry. Cryogenic electron tomography (cryo-ET) showed how COLVI wraps around the amyloid forming a helical superstructure, likely stabilizing and protecting the fibrils from clearance. Thus, here we report structural evidence of interactions between amyloid and collagen, potentially signifying a distinct pathophysiological mechanism of amyloid deposits.

Systemic AL amyloidosis is a rare plasma cell dyscrasia with an annual incidence of about 12–15 new cases per million people¹. AL amyloidosis is due to the overexpression of an amyloidogenic LC that misfolds and forms amyloid deposits in several organs². The circulating LC molecules exert proteotoxicity which concurs with the mass effect produced by amyloid deposits to fatal organ dysfunction¹. Due to genomic recombination and somatic mutations every AL patient bears a virtually unique amyloidogenic LC sequence, originating from either the λ - or κ -gene locus^{3,4}. Most patients are affected by deposits in multiple

organs, but heart manifestation dictates the prognosis in ~75% of cases^{5–9}. Without its associated heavy chain, free LCs fold into homodimers where each monomer consists of an N-terminal variable domain (V_L) and a C-terminal constant domain (C_L) connected by a flexible joining region^{10–13}. While free LCs are eliminated rapidly under healthy conditions, abnormal levels of an amyloidogenic LC cause vast accumulations of cross- β amyloid fibrils in AL amyloidosis^{1,4}. Cryo-EM has emerged as a powerful method to determine molecular structures of ex vivo amyloids, retrieved from patients affected by various

A full list of affiliations appears at the end of the paper. ✉ e-mail: stefano.ricagno@unimi.it

amyloidoses^{15–21}. The structures of fibrils from cardiac tissue of four AL patients, denoted as λ 6-AL55, λ 3-FOR005, λ 1-FOR001, and λ 1-FOR006, display distinct folds^{3,15–19}. So far, only residues belonging to V_L were found in the structured core of the AL amyloid, resulting in high sequence variability in the core of the deposited fibrils^{3,15–19}. Structures of sequence-identical amyloid from the heart and kidney of the same patient are well superposable, indicating a crucial role of the V_L sequence in determining the fibrillar structure¹⁹. Other sources of variability in this disease are post-translational modifications (PTM), and in particular proteolytic processing and N-glycosylation hotspots. The latter were shown to correlate with AL onset for κ LCs^{22–24}. To date, glycosylation in λ LCs is not considered a risk factor for AL^{24,25}, but the cryo-EM structure of λ 1-FOR001 shows a covalently linked glycan that may impact the resulting amyloid fold¹⁸.

Ancillary proteins are reproducibly found in amyloid deposits, including heparan sulphate proteoglycan, serum amyloid P-component and various extracellular matrix elements (ECM) such as collagen^{1,26–30}. The ECM provides structural support for organs and tissues and is dynamically remodelled, controlling tissue homeostasis and modulating immune cell responses^{31–33}. As most prominent ECM component, collagens are frequently detected in deposits extracted from different amyloidosis types²⁷. Collagen interactions seem to affect directly amyloid formation and disease progression^{27,34–40}. Collagens facilitate misfolding of native human β_2 -microglobulin (β_2 m) into amyloid, leading to fibril deposition in the joints of haemodialyses patients^{36–39}. Increased collagen content was found in cerebral microvessels of patients with Alzheimer's disease, and a neuron-protective role was put forward for COLVI^{41–43}. Recent evidence suggests that binding of collagens in general, but particularly COLI and COLIV, protects AL amyloid against phagocytic clearance in experimental mouse models^{34,35}. Thus, collagen/amyloid interactions modulate the progression of various amyloidoses.

Here we report the 3.6 Å resolution cryo-EM structure of N-glycosylated AL amyloid, which was extracted from the heart of a patient with cardiac AL amyloidosis and is referred to as AL59. AL59 is, to the best of our knowledge, the first AL amyloid structure with an extended constant domain fragment in its fibril core. The fold is related to that of a previously reported AL amyloid structure, belonging to the same λ 3-gene subfamily. Ex vivo AL59 fibrils display the unique ability to interact with a polymer from the extracellular matrix, which was identified as COLVI. While COLVI was not resolved in the helical reconstruction of the amyloid, we applied IEM and cryo-ET to reveal that COLVI wraps helically around the fibril, potentially stabilising and protecting AL59 amyloids from macrophage recognition.

Results & discussion

Ex vivo AL59 amyloids form abundant complexes with co-purified unknown polymer

AL59 amyloids were extracted from the heart apex tissue of a 56 years old woman, who had died from progressive heart failure and systemic AL amyloidosis (Supplementary Fig. 1 and Supplementary Tab. 1). The amyloid extraction procedure is standardised in our laboratory as previously described^{16,28,44}. AL59 belongs to the λ 3 light chain family, and is more specifically encoded by the variable gene *IGLV3-01*, and *IGLJ2*01* for the joining segment. Liquid chromatography tandem mass spectrometry (LC-MS/MS) carried out on extracted fibrils revealed peptide fragments corresponding to residue numbers 1–204 of AL59 (Supplementary Fig. 1). To determine the molecular structure of AL59 amyloids, cryo-EM data were collected. Inspection of raw cryo-EM micrographs of the vitrified amyloid extract revealed fibrils with an alternating width pattern, from which we estimated a crossover length of ~1200 Å (Fig. 1a). Surprisingly, an additional polymer distinct from amyloid was abundantly present in all fibril samples extracted from AL59 cardiac tissue (Fig. 1a). This polymer was present both in isolated form and also AL59-associated. In its unbound form, the polymer exhibits a bipartite repeating structure comprising 500 Å long beads connected by 600 Å long and 50 Å thin fibres, thus exhibiting a periodicity of 1100 Å (Fig. 1a). With further micrograph inspection, we also recognised the same bead-like shape as part of the amyloid-decorating polymer (Fig. 1a). Among 184 micrographs with higher visual contrast, we found the polymer decorating about 80% of amyloid fibrils. To unveil the structural properties of this unique AL59/polymer complex, we also collected cryo-ET data. In agreement with the cryo-EM micrographs, tomograms revealed undecorated amyloid, free polymer, as well as abundant polymer-decorated amyloid (Fig. 1b).

The structure of glycosylated AL59 is double-layered and adopts a u-shaped core that is closed by a β -arc segment and extended by a straight tail

To determine the structure of AL59, free and polymer-decorated amyloids were picked as single population for standard helical reconstruction^{45,46}. A reference-free 2D class average of particles extracted with a box size of ~1600 Å confirmed the estimated crossover length of ~1200 Å (Supplementary Fig. 2a). Class averages of particles extracted with a smaller box size of 302 Å, revealed the amyloid-characteristic β -spine (Supplementary Fig. 2b). The 2D class averages were characteristic of amyloid, lacking any features attributable to the abundant polymer.

From the initially extracted ~240 k particles, ~38 k were reconstructed to a final map with a resolution of 3.6 Å (Fig. 2a). Based on the AL59 amino acid sequence, we built the entire structure unambiguously into the continuous density, starting from the disulphide bond between residues Cys-22 and Cys-87 (or Cys-23 and Cys-88 according to Kabat numbering of antibodies, see Supplementary Tab. 3), clearly marked in the map (Fig. 2a). The single proto-filament of the built model comprises residues 1–118, 51 of which form 9 β -strands (Fig. 2b).

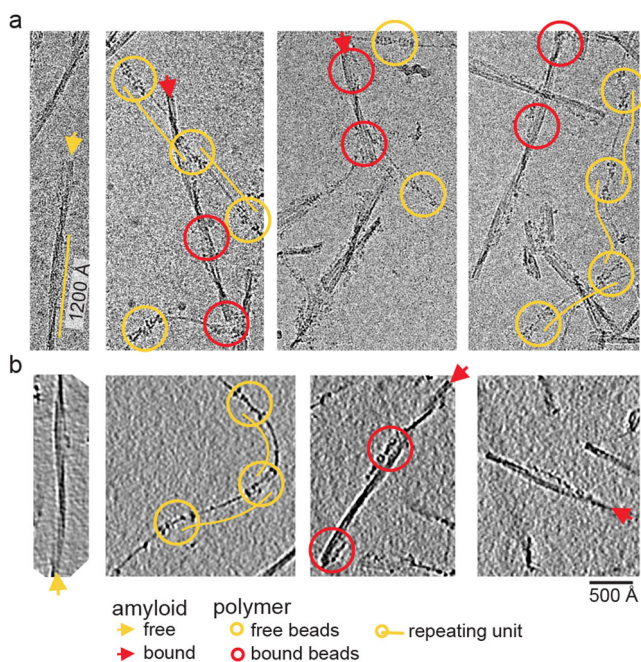


Fig. 1 | AL59 extract comprises additional polymer decorating the amyloid fibrils. a Cryo-EM micrographs and **b** Cryo-ET 2D projections reveal undecorated and polymer-decorated AL59 fibrils, highlighted by yellow and red arrows, respectively. The remarkably shaped polymer beads are encircled in yellow and red for the unbound and amyloid-associated forms, respectively. A thin yellow line indicated the estimated crossover-length. The image scale-bar is valid for both panels. See Supplementary Fig. 1.

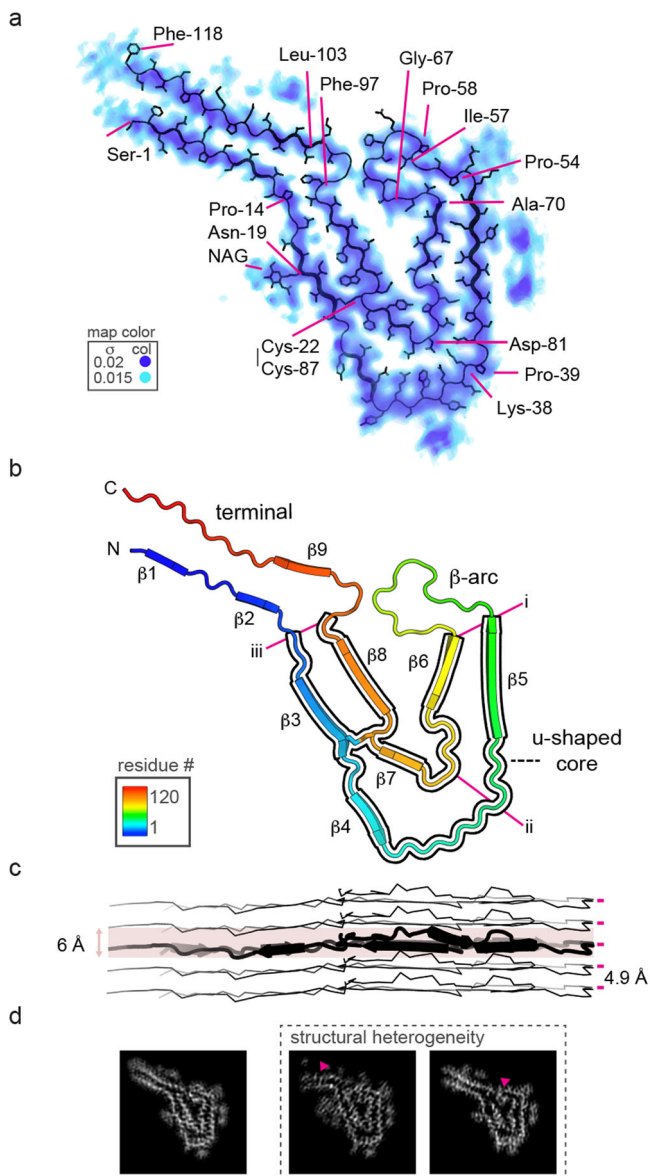


Fig. 2 | The structure of glycosylated AL59 exhibits a meandering double layer comprising a central β -arc, u-shaped core and a terminal straight segment.

a Cross-sectional view of the reconstructed map, visualised according to the depicted σ -colour scale. The polypeptide backbone and side-chains of the models are shown as black cartoon and sticks, respectively. **b** The polypeptide backbone is shown as cartoon, coloured on a rainbow-spectrum for residue numbers from 1 to 120. The three kinks are highlighted as pink straight lines. The u-shaped core is highlighted by a black outline. The terminal and β -arc segments are labelled. **c** Side-view of the deposited model comprising five subunits. The height difference of the polypeptide layer is indicated for the central layer, highlighted as thick ribbon. **d** -5 \AA cross-sectional slices through the reconstructed AL59 map are shown applying a black/white (0/0.09) linear scale (left). The structural heterogeneity panel depicts two additional alternative conformations of AL59 amyloid core (highlighted by pink arrow) that emerged during 3D classifications.

A central β -arc segment folds the proto-filament into a meandering double layer with three sharp kinks, marked by residue pairs (i) Pro-54/Ala-70, (ii) Pro-39/Asp-81 and (iii) Pro-14/Phe-97 (Fig. 2b). The double-layer between the first and third kink adopts a u-shaped core structure. The opposing N- and C-terminal tails follow a straight path and are kept close by hydrophobic interactions (Supplementary Fig. 3). Viewed along its long fibril axis with a helical rise of 4.9 \AA , a single layer appears rather compact exhibiting maximal $C\alpha$ height differences of -6 \AA

(Fig. 2c). An additional density around Asn-19 was modelled as N-linked N-acetyl glucosamine (NAG), as glycosylation was also detected by mass spectrometry, 2D-PAGE and western blot (Fig. 2a, Supplementary Fig. 1). N-glycosylation has been reported to correlate with amyloidogenic κ , but not λ LCs^{24,47}. Curiously, among the five ex vivo LC amyloid structures^{3,15-19}, AL59 is the second with a structurally confirmed glycosylation site, indicating that glycosylation of λ -LCs may be more common than expected.

Two additional structures displaying alternative conformations of AL59 emerged in 3D classifications, thus indicating structural heterogeneity of the fibrils (Fig. 2d). However, their reconstructions reached only -3.9 \AA resolution and the obtained maps featured main chain breaks, thus hindering us to build a molecular model and to interpret these structures in detail.

In summary, the structure of glycosylated AL59 displays a double-layered u-shaped core with a β -arc lid and a straight tail extension.

AL59 adopts a fold related to λ 3-FOR005, but harbours an extended constant domain fragment in its amyloid core

In keeping with the four other reported ex vivo LC amyloid structures (Fig. 3a)^{3,15-19}, AL59 adopts a fold substantially different from its native structure (Fig. 3b), but retains the conserved disulphide bond between Cys-22 and Cys-87. The 59-64% sequence-identical V_L -domains of the λ 1- and λ 6-subfamily members (Fig. 3a) adopt amyloid folds different from AL59. Interestingly, the structure of the \sim 70% sequence-identical and non-glycosylated λ 3-FOR005 is superimposable on the AL59 structure with a root mean square deviation of $\sim 4 \text{ \AA}$ over 81 aligned residues (Fig. 3a, c). The two related folds exhibit similar positioning of the disulphide bond and CDR segments (Fig. 3c). Glycosylation does not seem to impact this specific amyloid fold. In contrast, the authors of a previous study suggested that glycosylation of λ 1-FOR001 contributes to define its specific amyloid fold¹⁸. Thus, here we show that two LCs belonging to the same germline subfamily, but from different individuals, adopt a related amyloid fold. This observation corroborates our previous findings of identical structure of fibrils extracted from different organs of the same individual, indicating that the fibril fold is dictated by its primary sequence¹⁹.

In contrast to the previously reported LC amyloid structures^{3,15-19}, AL59 is to the best of our knowledge the first structure with a C_L domain fragment extending beyond residue position 106, that is located within the V_L - C_L joining region. A model for LC amyloid aggregation posits that proteolytic cleavage of the joining region is required to trigger fibril formation by the amyloidogenic V_L domain molecules^{48,49}. Evidently, such a model cannot be applied to AL59 amyloid aggregation. If a proteolytic event is necessary to destabilise AL59 native fold, it may occur in the C_L domain. Furthermore, we applied our established LC-MS/MS protocol which revealed proteolysis hotspots in the C_L domain of AL59 (Fig. 3b), similarly to those reported for λ 6-AL55 and λ 1-H7^{28,44}. These observations support our previous interpretation that in vivo proteolysis occurs mostly *post* aggregation^{28,44}.

Thus, λ 3-AL59 amyloid adopts a fold related to LC fibrils derived from the same germline subfamily, regardless of originating from a different patient. The inclusion of an extended C_L -derived fragment in the AL59 amyloid core, combined with the extensive fragmentation of the C_L domain, point at the C_L domain as main target for in vivo proteolysis.

Collagen VI is co-extracted with AL59 fibrils from cardiac tissue

To facilitate identification of the additional polymer observed in the micrographs, 2208 beads (Fig. 1a) were picked manually for single-particle analysis (SPA). 2D class averages of the beads revealed two half-beads, each $\sim 140 \text{ \AA}$ wide and $\sim 165 \text{ \AA}$ long, connected by a $\sim 20 \text{ \AA}$ wide and $\sim 90 \text{ \AA}$ long intra-bead fibre (Fig. 4a, Supplementary Fig. 4b). The two half-beads adopt non-identical orientations, rotated around the intra-bead fibre. Each half-bead exhibits a tripartite structure with a

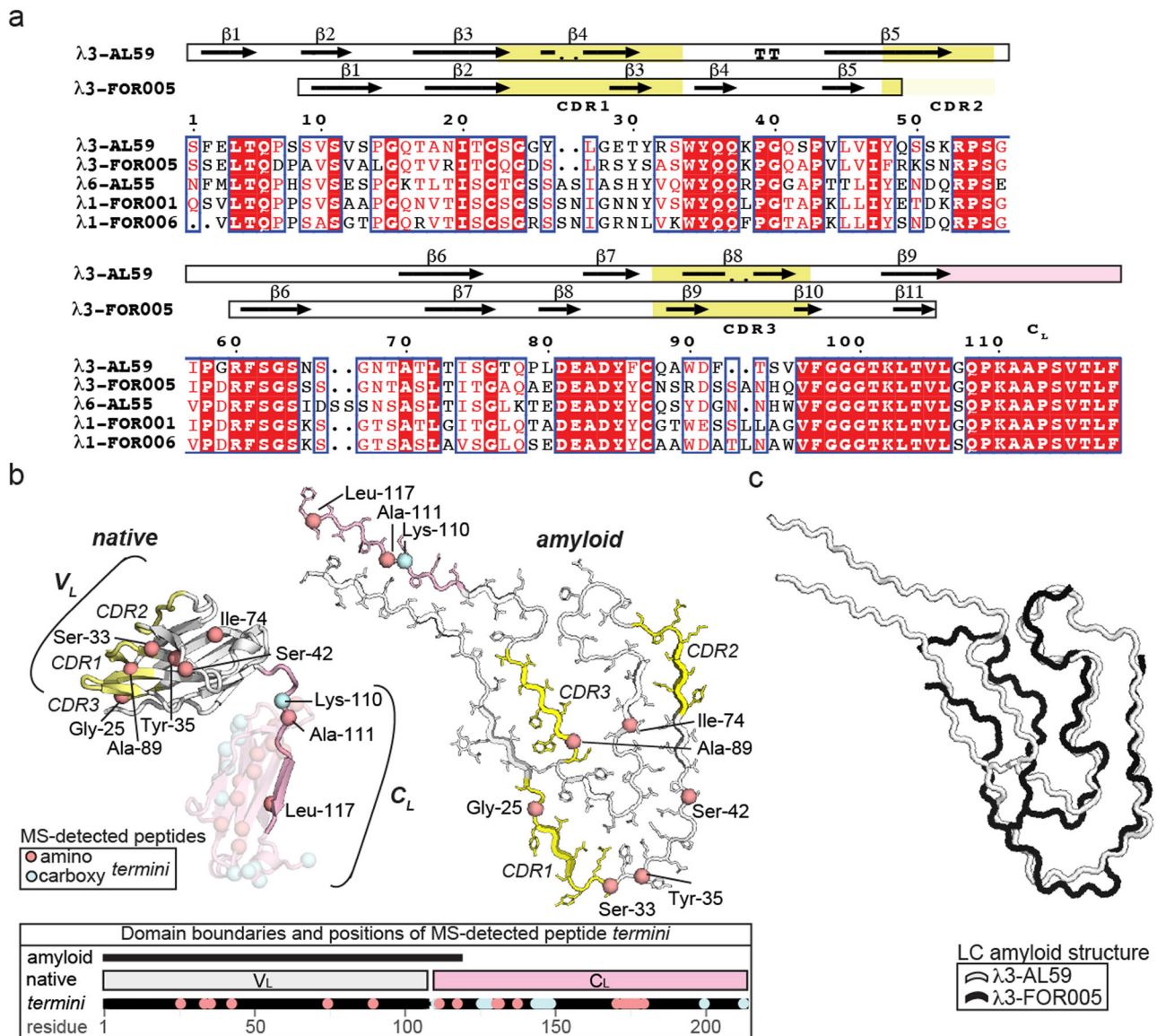


Fig. 3 | AL59 adopts a fold related to λ3-FOR005, but harbours an extended constant domain (C_L) fragment in its amyloid core. **a** Sequence alignment of AL59 belonging to the λ3 gene to the four other ex vivo LC amyloid structures λ3-FOR005 [https://www.rcsb.org/structure/6Z10], λ6-AL55 [https://www.rcsb.org/structure/6HUD], λ1-FOR001 [https://www.rcsb.org/structure/7NSL] and λ1-FOR006 [https://www.rcsb.org/structure/6IC3]. β-strands and strict β-turns are indicated by numbered β and non-numbered TT symbols, respectively. Strict sequence identity is indicated by a red box with white character, similarities within and across groups are indicated by red characters and blue frames, respectively. Secondary structure elements of λ3-AL59 and λ3-FOR005 are shown above. CDR

segments of λ3-AL59 and λ3-FOR005 are labelled and highlighted in yellow and orange, respectively. The C_L-derived fragment in the amyloid core of AL59 is highlighted in light pink. **b** The AI-generated native AL59 structure (left) is compared to the amyloid structure (right). V_L and C_L domains are coloured white and light pink, respectively. The CDRs are coloured yellow and labelled. The non-amyloidogenic C_L part is semi-transparent. Modified N- and C-termini of LC peptide fragments detected by LC-MS/MS are shown as red and blue Cα-spheres, respectively. The residue-level line-plot depicts the domain boundaries and modified N- and C-termini of LC fragments detected by LC-MS/MS. **c** The superimposed λ3-AL59 and λ3-FOR005 structures are shown as white and black cartoons, respectively.

head, an intermediate central body, and two tails lining the intra-bead fibre (Fig. 4a). Inter-bead fibres were apparent, but not well resolved. Our search for a polymer with matching structure was facilitated by LC-MS/MS identification of collagen VI (COLVI) subunits α1, α2 and α3 as major components in the AL59 extract (Supplementary Tab. 4). The structural organisation of the abundant polymer was matched visually to the previously described unique architecture of COLVI bead-on-a-string microfibrils^{50–55}. In line with the posited COLVI assembly model (Supplementary Fig. 4a), integrated from biochemical and structural results collected over decades^{50–54,56,57}, the two half-beads appear two-fold symmetric in reference-free 2D class averages (Fig. 4a). Focused heterogeneous 3D refinement of C2 symmetry-expanded half-beads yielded a 13 Å resolution map (Fig. 4b and Supplementary Fig. 5), with

an overall shape reminiscent to that of COLVI from *bovine corned*⁵². As predicted by the assembly model, additional two-fold symmetry splits the half-beads into quarter-beads (Supplementary Fig. 5). While enforced symmetry improved the FSC-based resolution estimate to 12 Å, map interpretability was not markedly improved.

In summary, our single particle cryo-EM and LC-MS/MS data allowed us to identify the co-purified abundant polymer in the AL59 amyloid extract as COLVI.

COLVI forms helical superstructures with AL59 fibrils

To unambiguously identify COLVI as the AL59-decorating polymer, we performed IEM applying a COLVI-specific⁵⁸ polyclonal antibody followed by gold-conjugated secondary antibody staining of the same

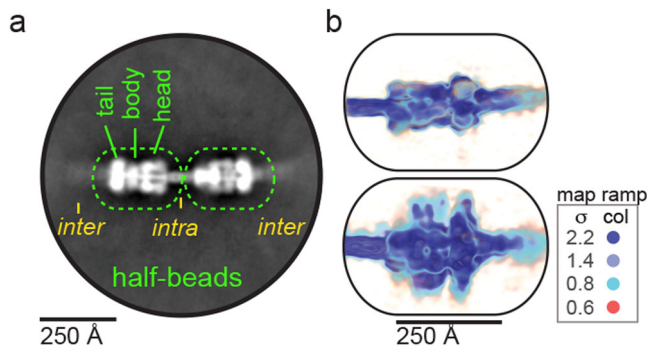


Fig. 4 | Collagen VI is the abundant polymer concatenating with AL59. **a** The 2D class average reveals two half-beads linked by an intra-bead fibre. Each half-bead entails head, body and tail substructures. Inter-bead fibres appear blurry, likely due to high flexibility. **b** Two views of the half-bead map that is visualised according to depicted σ -colour scale. The main features (darker blue) are comparable to a map at a threshold of 1.5 σ . See Supplementary Figs. 4 and 5.

extract used for cryo-EM and cryo-ET sample preparations. The IEM images revealed single amyloid fibrils, amyloid clusters and free COLVI polymers tagged by gold (Fig. 5a and Supplementary Fig. 6). Gold particles were located within distances of ~ 150 Å to single AL59 fibrils, corresponding to half the theoretical length of two coupled antibodies, thus marking complexes between AL59 and COLVI and identifying COLVI beads. Gold duplets with centre-to-centre distances of ~ 240 Å possibly mark two distinct quarters within the same full-bead of COLVI. When the same sample was treated only with gold-conjugated secondary antibody, no gold particles were found (Fig. 5a and Supplementary Fig. 7).

COLVI was not observed in the helical reconstruction of AL59, likely due to the helical symmetry applied during the reconstruction procedure. The repeat distance of the amyloid building block is ~ 5 Å, while this value is 1100 Å for COLVI-beads. Indeed, applying SPA we obtained a single 2D class average from 78 non-duplicated particles, which might be interpreted as amyloid with associated COLVI-bead (Supplementary Fig. 4c).

To better characterise the architecture of unique AL59/COLVI complexes, we applied cryo-ET (Figs. 1b and 5b). In the reconstructed tomograms, the majority of AL59 was decorated by COLVI (Fig. 5b). Generally, the rigid AL59 fibrils were better defined than the heterogeneous COLVI decorating density. Thus, although we observed bead-like structures in amyloid-associated COLVI (Fig. 1b), our attempts to average sub-tomograms were not successful, preventing a molecular reconstruction of the AL59-COLVI complex. Notably, COLVI wraps around the central AL59 fibril, adopting the helical twist and rise values of the amyloid but with a three times larger helical radius (Fig. 5b). While COLVI adopts a non-helical superstructure on its own, the amyloid fibril imprints its helical structure on COLVI, resulting in complexes with an interaction interface spanning for thousands of angstrom. Such a chirality transfer is regarded as fundamental mechanism across scales in natural and artificial systems^{59–62}. Specifically amyloids, exploited in nanotechnology and biotechnology, were reported as chirality inducers^{60,63,64}.

Recently, collagen was reported to play a protective role against amyloid clearance by macrophages^{34,35}. The helical superstructures between AL59 and COLVI with such extensive interaction surfaces can exemplify how collagen may contribute to amyloid stabilisation and may hide misfolded aggregates from macrophage activity^{34,35}. Earlier studies have also demonstrated adverse effects of collagen in various other amyloidoses. In dialysis-related A β 2 M amyloidosis, collagen facilitates β 2 m aggregation and interacts weakly with mature β 2 m fibrils^{36–39}. In ATTR amyloidosis, transthyretin (TTR) tends to aggregate in the presence of basement membrane components such as collagen

IV, whose expression correlates with amyloid accumulation^{65,66}. Collagen levels are also increased in the brains of Alzheimer's patients where collagen seems to play a neuroprotective role and facilitates the formation of mature A β fibrils^{41–43,67}. Then why had no structural evidence of such interactions been reported to date? A possible answer is that these interactions are typically weak and do not withstand the forces exerted during extraction. The unexpected abundance of COLVI in our micrographs may be related to unique amyloid features. LC fibrils in different AL patients present distinct surface residues, thus forming intermolecular complexes with variable stability. By serendipity, AL59 amyloids can interact strongly with COLVI, resulting in the abundant and reproducible observation of the AL59/COLVI complex in our ex vivo extracts. Moreover mild extraction protocols may facilitate the observation of such complexes. Remarkably, a micrograph of λ 3-FOR005, shown in Supplementary Fig. 1 of that study¹⁵, displays an amyloid-concatenated polymer resembling COLVI. Thus, the concatenation of amyloid with collagen, exemplified here as helical superstructures, may represent a general mechanism by which collagen(s) could modify the recognition of amyloid by host defence mechanisms.

In summary, here we report the cryo-EM structure of AL59 amyloids extracted from an AL patient with severe cardiac involvement. Glycosylated λ 3-AL59 adopts a double-layered structure featuring a u-shaped core with a β -arc lid and a straight tail extension. AL59 is to the best of our knowledge the first LC amyloid structure comprising a C_L domain fragment, thus incompatible with the model suggesting that LC amyloids are formed by isolated V_L domains released upon LC proteolysis. Surprisingly, AL59 fibrils form helical superstructures with COLVI, representing evidence of a stable interaction between amyloid and ECM components. This observation provides insights about the potential role of collagen as a modulating agent of amyloid deposits, potentially signifying a distinct pathophysiological mechanism for amyloidoses.

Methods

Ethical statement

This study was approved by the Ethical Committee of Fondazione IRCCS Policlinico San Matteo and was performed in accordance with the Declaration of Helsinki. Data were collected from the Ethics Committee approved ReAL amyloidosis registry (NCT04839003). We have written consent of the patient to publish clinical information potentially identifying the individual.

Clinical characteristics of patient AL59. Patient AL59 was affected by AL amyloidosis with cardiac involvement and died of progressive heart failure. After autopsy examination, showing Congo red positivity in heart, tissue was stored frozen (-80 °C) without fixation until use. AL amyloidosis had been diagnosed 10 months earlier on abdominal fat aspirate, where amyloid deposits were evaluated by Congo red staining under polarised light and amyloid typing was confirmed by immuno-electron microscopy⁶⁸. Organ involvement was defined according to international criteria⁶⁹. Baseline clinical and demographic information are listed in Supplementary Tab. 1. The patient was treated with cyclophosphamide, bortezomib and dexamethasone. After four cycles, haematologic partial response was reached (dFLC levels declined from 280 to 111 mg/L), with cardiac progression (NT-proBNP levels rose from 6043 to 17,600 ng/L). Treatment was subsequently stopped for progressive heart failure.

cDNA sequencing of monoclonal LC (Pavia). Total RNA was extracted from 10^7 bone marrow mononuclear cells using TRIzol reagent (Life Technologies, Paisley, United Kingdom). Nucleotide sequence of monoclonal LC variable region (V_L) was cloned by a universal inverse-PCR strategy that preserves its original sequence at 5' and 3' ends⁷⁰. Briefly, primers specific for the 5' (λ -C_{LA}: 5'-AGTGTGGCCTTGTTGGCTTG-3') and 3' (λ -C_{LB}: 5'-GTCACGCATGAAGGGAGCAC-3') ends of

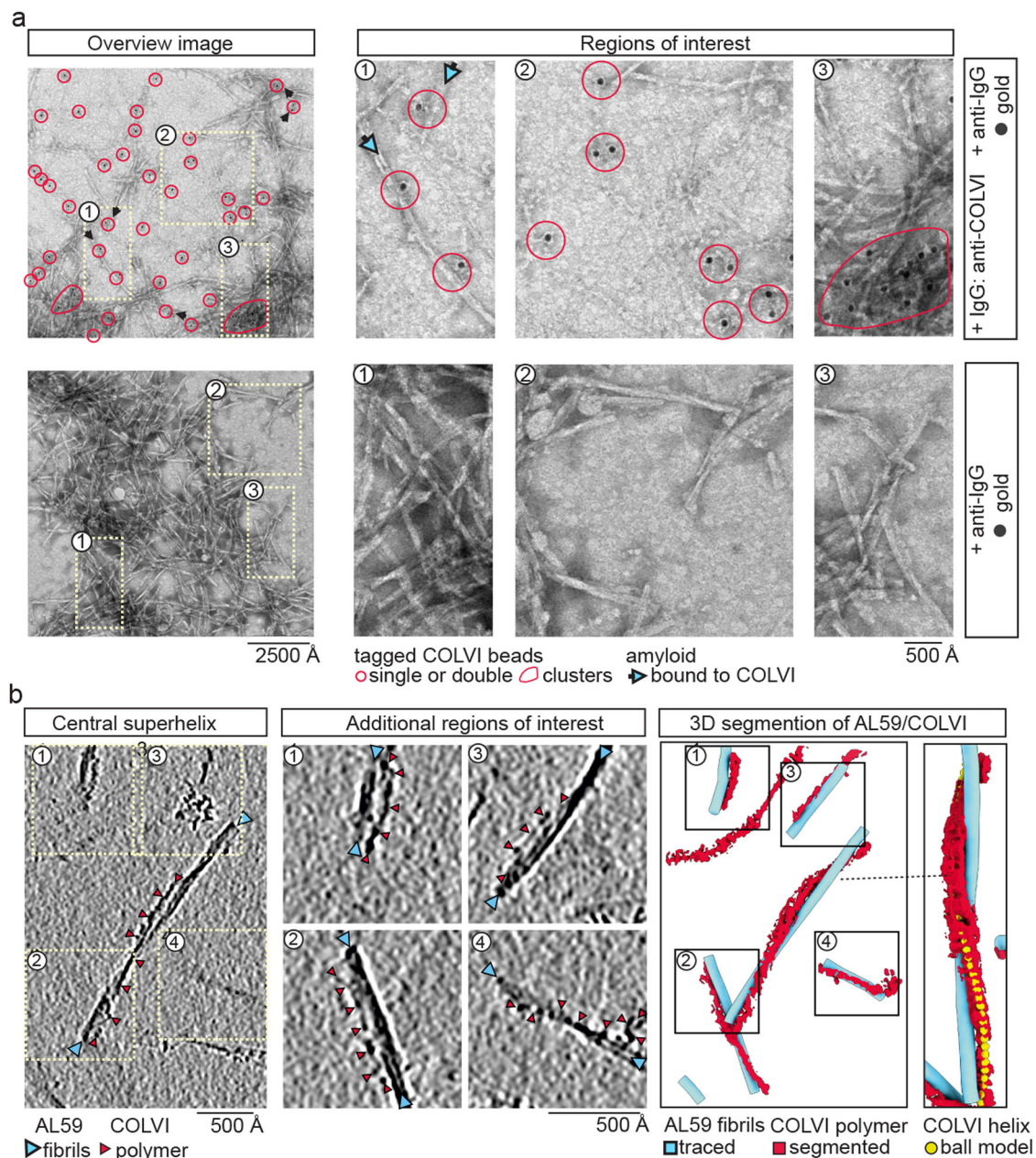


Fig. 5 | The fibril-decorating polymer is COLVI and follows the helical pitch of AL59. **a** Immuno-electron microscopy (IEM) revealed AL59 fibrils, free polymer and dense fibril clusters tagged with gold particles. *Top panel:* > 50 gold particles, highlighted in red, were counted in this image of the extract stained with anti-COLVI IgG and gold-conjugated anti-IgG antibodies 70R-CR009x (Fitzgerald) followed by a 12 nm gold-conjugated anti-IgG antibody, respectively. Three magnified sections emphasise (1) three gold particles within ~150 Å distance to AL59 fibrils, (2) three single gold particles and three duplets tagging free COLVI polymer as well as (3) 11 gold particles within a dense amyloid fibril cluster. *bottom panel:* No gold particles were found in the sample treated only with the gold-conjugated anti-IgG antibodies. Three magnified sections are shown for direct comparison to the top

panel. See Supplementary Figs. 6 and 7. **b Left:** An overview cryo-ET slice with a thickness of 0.925 nm and four additional regions of interest (highlighted boxes) reveal amyloid fibrils (blue arrowheads) decorated with COLVI polymers (red arrowheads). The height level of the overview slice highlights the central AL59/COLVI interaction. The four boxes are shown at different height levels and higher magnification. **Right:** 3D renderings of the overview cryo-ET slice and the highlighted central AL59/COLVI interaction show traced AL59 fibril tubes (blue) decorated with segmented COLVI densities (red). A helical ball model (yellow) with helical twist and rise of AL59, but three times larger helical radius, is shown within the COLVI density to demonstrate the helical imprinting of AL59 on COLVI.

the λ -LC C_L were used. The PCR fragment was ligated into a cloning vector and amplified. After plasmid purification, insert was sequenced to deduce the V_L chain sequence. To determine the germline of AL59- V_L , the sequence was aligned to the EMBL-GenBank, V-BASE (V BASE Sequence Directory, MRC Centre for Protein Engineering, Cambridge, UK) and IMGT sequence directories. The sequence showed the highest homology with the *IGLV3-1* and *IGLJ2*0* germline gene. The AL59- V_L

sequence was deposited in the GenBank database (GenBank OR567864).

Fibril purification from heart tissues of patient AL59. Fibrils were extracted from 500 mg of autaptic heart tissue (apex) as previously described¹⁶, obtaining six consecutive water-extracted fractions of 750 μ l each. To evaluate the yield, 50 μ l of each fraction were vacuum dried

and re-suspended in 20 μ l of 8 M urea to solubilise the fibrils. After protein quantification, using microBCA assay (Thermo Fisher Scientific), fibril patterns were analysed by SDS-PAGE under denaturing and reducing conditions. Water extract fraction #3 was selected for proteomic and cryo-EM analyses.

N-glycosylation proteomic analyses by PNGase F digestion. For western blot and LC-MS/MS analyses protein was deglycosylated using PNGase F (New England Biolabs) under denaturing and non-denaturing (glycerol-free) conditions, respectively²⁴, according to the manufacturer's instructions. Control samples were prepared by replacing enzyme with water.

Proteomic characterisation of enriched amyloid fibrils derived from heart tissues of patient AL59. About 250 mg of heart tissue (apex) were used for the fibril enrichment procedure, performed on ice and in presence of protease inhibitors. The obtained pellet was characterised for LC fragments as described previously^{28,44}. Briefly, 2D-polyacrylamide gel electrophoresis was performed under denaturing and reducing conditions. Proteins were detected using GelCode™ Blue Stain Reagent (Pierce). Subsequently, glycoproteins were revealed on the same gel as magenta spots applying the Glycoprotein Staining Kit (Pierce) according to manufacturer's instructions. LCs were identified by western blot, using polyclonal rabbit anti-human λ LC antibody (1:25,000, A0914, Dako). To identify the N- and C-“terminomes” of LC proteo-forms in the amyloid fibrils^{24,28}, bottom-up proteomic analysis was performed on proteins chemically derivatized at the N- and C-termini by dimethyl labelling and amidation with ethanolamine, respectively.

Liquid chromatography – tandem mass spectrometry (LC-MS/MS) analysis and database search. LC-MS/MS analyses were performed on a Dionex Ultimate 3000 nano-UHPLC RSLC system coupled to a Q Exactive Plus mass spectrometer (Thermo Fisher Scientific, Waltham, MA, USA) equipped with an EASY-spray ion source (Thermo Fisher Scientific). Peptides were washed on a trap column (PepMap100 C18, 0.3 \times 5 mm, 5 μ m, 100 \AA , Thermo Fisher Scientific) and separated on an analytical column (PepMap RSLC C18, 75 μ m \times 50 cm, 2 μ m, 100 \AA , Thermo Fisher Scientific). Raw data were processed using the Sequest HT search engine contained in the Proteome Discoverer software, version 2.0 (Thermo Scientific). Peptide searches were performed against the human proteome (UniProt [<https://www.uniprot.org/>]) and internal common contaminants databases, supplemented with the AL59 sequence determined in this study. Matching the obtained peptides to the available λ -C₁ sequences in the UniProt database, the AL59 C₁-domain was identified. Further detailed about the C- and N-termini labelling and N-glycosylation proteomic analyses were described previously^{24,28}. In all database searches semi-tryptic peptides were considered. Since N-glycan removal leads to deamidation of asparagine, the N-glycosylation site was evaluated by comparison of peptides carrying deamidated asparagine in PNGase F digested and in control sample. All spectra assigned to peptides containing Asp-19 were manually checked.

Electron microscopy (EM)

Negative stain. To evaluate the quality and concentration of amyloid, extracts were analysed by negative stain EM, as described previously¹⁶. Grids were imaged on a Talos L120C transmission electron microscope (Thermo Scientific) operating at 120 keV.

Single-particle cryo-EM sample preparation and data collection. Samples were mixed by vortexing for 10 s at room temperature. Droplets of 3 μ l were incubated for 30 s on freshly glow-discharged holey thick carbon grids (C-flat 1.2/1.3 C, Protochips), and plunge-frozen in liquid ethane using a Vitrobot Mk IV (Thermo Fischer Scientific),

operated at 4 °C and 100% humidity. The main dataset comprising 2049 movies was collected automatically on a Talos Arctica 200 kV (Thermo Fisher Scientific), equipped with a Falcon 3 direct electron detector operated in electron counting mode (Supplementary Tab. 2). Movies were recorded at a nominal magnification of 120,000, corresponding to a pixel size of 0.889 \AA /pixel and a total dose of 40 e⁻/ \AA^2 , equally distributed over 40 fractions. A second dataset comprising 2556 movies was collected on the same microscope operated with the same settings, except for a lower magnification of \times 73,000 corresponding to a pixel size of 1.43 \AA .

Helical reconstruction AL59. The structure of AL59 was reconstructed following standard protocols in RELION 3.1^{45,46,71,72}. 1366 dose-weighted, motion- and CTF-corrected micrographs were selected from the main dataset based on a CTF-fitting resolution cut-off set to \leq 10 \AA . 5112 fibrils were picked start-to-end manually from the micrographs in RELION 3.1^{45,46,71,72}. A first set of 44,115 long segments was extracted with 1800-pixel box-size, binned by 6, and an inter-box distance of 30 \AA . The tube diameter was set to 150 \AA . A single reference-free 2D class average was used for initial model generation following published protocols⁴⁵, by applying an estimated crossover distance of 1200 \AA (Supplementary Fig. 2a). Extraction of short segments with a 340 pixel box-size and inter-box distance of 15 \AA yielded 240,985 segments. Reference-free 2D classes obtained with a regularisation value of $T = 8$ yielded averages with clearly visible cross- β structure (Supplemental Fig. 2b). The initial model was re-scaled and re-windowed to match the un-binned short segments and low-pass-filtered to 10 \AA .

Initial 3D auto-refinement applying C1 symmetry as well as helical twist and rise values of -0.7° and 4.9 \AA , respectively, yielded a 4.2 \AA resolution map. Initial 3D classification with a regularisation value of $T = 24$ yielded two structural classes comprising 54,825 (55k) and 31,113 (31k) particles, each displaying polypeptide features. 3D classification of the 55k particle-set showed two structures comprising 37,904 (38k) and 16,921 (17k) particles, respectively. The structure presented herein was reconstructed from the 38k particle-set by 3D auto-refinement applying a 5 \AA low-pass filtered reference map, 270 \AA mask, helical tube radius of 180 \AA and Z-value of 30%. Post-processing with a B-factor of -106\AA^2 yielded a 3.6 \AA resolution map, assessed using the 0.143 FSC threshold criterion (Supplementary Tab. 2). The two additional structures emerged early and late during reconstruction of the main structure. The early-emerging structure was reconstructed from 23,010 particles, selected by 3D classification of the initial 31k particle set. The late-emerging structure was reconstructed from 12,355 particles, selected by 3D classification of the later obtained 17k particle set. Both structures were 3D auto-refined using the same settings as for the main structure, and post-processed to yield 3.9 \AA resolution maps.

Model building of AL59. The initial model was built de novo in Coot⁷³, starting from the position of the disulphide bond between Cys-22 and Cys-87. The polypeptide backbone of the model was extended by placement of poly-Alanine residues into the continuous map. Considering bulky side-chain features, residues were mutated to match the AL59 protein sequence. The model was iteratively built and refined in Coot, Chimera-Isolde and Phenix real-space refinement with reference-model restraints^{73–76}. The additional density around Asn-19 was modelled as N-linked N-acetyl glucosamine (NAG), representing the first building block of the common N-glycan core⁷⁷. The final model comprising five 118-residue long chains in each proto-filament was obtained by refinement with additional non-crystallographic symmetry (NCS) restraints. Molprobit score and EMDb^{78,79} atom inclusion values of 1.56 and 0.74, respectively, suggest a physically valid model with good map support.

SPA of collagen VI. 1768 particles were picked manually in the micrographs of the main dataset with a pixel size of 0.889 \AA . The particles were extracted applying particle-box and diameter-

background sizes of 1126 and 844 pixels, respectively. To increase the number of particles, additional 1004 particles were picked manually from the second dataset with a pixel size of 1.43 Å. These particles were extracted applying particle-box and diameter-background sizes of 700 and 525, respectively. To match box- and pixel-size, the larger box was scaled to match the smaller one. After import of the particles into cryoSPARC⁸⁰, the particle box was scaled to 384 pixels, yielding a pixel size of 2.607 Å. The reconstructed ab initio map was refined homogeneously to an estimated resolution of 18 Å (Supplementary Fig. 5a and b). After map and particle re-orientation in ChimeraX⁷⁵, the number of particles was doubled by symmetry expansion and the map was subsequently refined locally to a resolution of 13 Å (Supplementary Fig. 5c). Enforced C2 symmetry during local refinement improved map resolution to 12 Å, but did not improve markedly map interpretability (Supplementary Fig. 5d). To estimate the available space of the quarter-bead volume, we placed 11 copies of an AI-model of α 2-VWFA2 [<https://www.uniprot.org/uniprotkb/P12110/entry>]. The crystal structure of a collagen triple helix [<https://www.rcsb.org/structure/1k6f>]⁸¹ was assembled into elongated parallel tetramers fitting snugly the volume of the intra-bead fiber.

Cryo-EM SPA of the AL59/COLVI complex. In Relion^{45,46,71,72}, 36,540 helical segments with a tube diameter of 500 Å were extracted from the manually picked 5112 fibrils, applying box-size and inter-box distance values of 840 and 84 pixels, respectively. The box was re-scaled to 280 pixels. Particles associated with their micrographs were imported into cryoSPARC⁸⁰ for 2D classification. Applying a maximum resolution of 10 Å, an initial classification uncertainty factor of 50, and a batch-size of 200 per class, the particles were sorted into 400 classes. Two classes comprising 119 particles were interpreted as amyloid with associated COLVI-bead. 37 particles with an inter-particle separation distance below 400 Å were removed as duplicates. 78 of the remaining 82 particles were aligned to yield the 2D class presented in Supplementary Fig. 4c. To provide a visual guide, the reconstructed map of the COLVI-bead was arranged with a surface of the AL59 fibril to match the shape of the 2D class average in ChimeraX⁷⁵.

Immuno-electron microscopy (IEM). 10 μ l drop of the AL59 extract were placed at room temperature for 30 min on a 200 mesh formvar/carbon coated nichel grid (EMS, Hatfield, PA, USA). After absorbing the excess of the suspension with Whatman filter paper, fibrils were then incubated with a rabbit anti-human collagen VI (1:10, Fitzgerald Industries International) overnight at 4 °C in a wet chamber, followed by a donkey anti-rabbit antibody conjugated to a 12 nm colloidal gold (1:75, Jackson Immunoresearch) in block solution for 45 min at 37°. After post-fixation with 2% glutaraldehyde, grids were finally negatively counterstained with 2% uranyl acetate and observed with an Energy Filter Transmission Electron Microscope (EFTEM, ZEISS LIBRA[®] 120) equipped with YAG scintillator slow scan CCD camera (Sharp eye, TRS, Moorenweis, Germany).

Cryogenic electron tomography (cryo-ET). Samples were prepared in the same way as for cryo-EM. Vitrified specimens were imaged on a Titan Krios cryo-transmission electron microscope equipped with a Selectris energy filter with a slit width of 15 eV and a Falcon IV direct electro detector (Thermo Fisher Scientific). Multiple tilt series with a pixel size of 2.32 Å were recorded over a tilt range of -54 to 54 degrees in 3-degree steps with a dose-symmetric scheme using SerialEM and PACE-tomo 1.2^{82,83}. The total electron dose was kept under 120 electrons/Å². Frames were aligned using MotionCor2 1.5.0⁷². Final tilt series were aligned using fiducial-less patch tracking, down sampled four times, and reconstructed into tomograms by back projection within IMOD 4.11.15⁸⁴. Contrast was enhanced by filtering the tomograms using CTF Deconvolve of isonet 0.2⁸⁵.

Tomograms were segmented using Amira (Thermo Fisher Scientific) as follows: amyloid fibrils were detected using Amira's XTTracing module based on cross-correlation with a cylindrical template (5 nm in radius and 25 nm in length). Cross-correlation fields were thresholded to balance the amount of true positives and negatives. Amyloid fibrils were then traced using a search cone 15 nm in length and 10° angle, with a direction coefficient of 0.3 and minimum fibril length of 25 nm. Decorating polymers as well as free COLVI were segmented manually. Pixels with a grey-scale value close to that of the solvent were filtered out using a threshold. Images of the three-dimensional rendering were produced in ChimeraX⁷⁵. To investigate whether amyloid-bound COLVI polymers adopted the same or a different helical symmetry than the amyloid, a ball model was constructed with helical twist and rise of AL59 but larger radius (60 Å) using SPIDER 26.06⁸⁶. For better visualisation, balls were displayed only every tenth AL59 subunit. Visual inspection revealed an almost complete overlap between the COLVI density and the helical model.

Data analysis and visualisation

Structures and derived data were analysed and visualised using Arpeggio and FATCAT web servers as well as Rstudio, ChimeraX^{75,87-90} and PyMol (Schrödinger, NY, USA). For the alignment of the AL amyloid sequences shown in Fig. 3a, C_L sequences of λ 1-FOR001 and λ 1-FOR006, reported to residue Ser-114⁴⁸, were extended to Phe-118 based on aligned⁴³ precursor sequences [<https://www.ncbi.nlm.nih.gov/protein/S05270>] and [<https://www.ncbi.nlm.nih.gov/protein/ANN81987.1?report=genpept>], respectively. Sequences were aligned and visualised using Uniprot, Blast, ClustalOmega and ESPript⁹¹⁻⁹⁴.

Statistics and reproducibility

The cryo-EM micrograph excerpts shown in Fig. 1a were selected from the main dataset comprising 2049 movies. The representative cryo-ET images shown in Figs. 1b and 5b were selected from 125 tomograms, 33 of which comprised collagen-concatenated amyloid. The IEM images shown in Fig. 5a were selected from in total 74 images.

Reporting summary

Further information on research design is available in the Nature Portfolio Reporting Summary linked to this article.

Data availability

The AL59-VL sequence was deposited in GenBank under accession code OR567864 [<https://www.ncbi.nlm.nih.gov/nucleotide/OR567864>]. The mass spectrometry proteomics data have been deposited to the ProteomeXchange Consortium via the PRIDE partner repository⁹⁵ with dataset identifiers PXD049301 and PXD049369. Source data relevant to Supplementary Fig. 1d are provided with this paper. The PDB and EMDB accession codes of the AL59 amyloid are 9FAA and EMD-50270, respectively. The raw cryo-EM images used in our SPA analysis were deposited in EMPIAR under the accession code EMPIAR-11408. The COLVI map was deposited under EMD-18689. The cryo-ET data were deposited under EMD-51031, EMD-51032, EMD-51033 and EMD-51038. Source data are provided with this paper.

References

- Merlini, G. et al. Systemic immunoglobulin light chain amyloidosis. *Nat. Rev. Dis. Prim.* **4**, 1–19 (2018).
- Merlini, G. AL amyloidosis: from molecular mechanisms to targeted therapies. *Hematol. Am. Soc. Hematol. Educ. Program* **2017**, 1–12 (2017).
- Haupt, C. The AL amyloid fibril: looking for a link between fibril formation and structure. *Hemato* **2**, 505–514 (2021).
- Del Pozo-Yauner, L. et al. Role of the mechanisms for antibody repertoire diversification in monoclonal light chain deposition

- disorders: when a friend becomes foe. *Front. Immunol.* **14**, 1203425 (2023).
5. Bodi, K. et al. AL-Base: a visual platform analysis tool for the study of amyloidogenic immunoglobulin light chain sequences. *Amyloid* **16**, 1–8 (2009).
 6. Perfetti, V. et al. The repertoire of λ light chains causing pre-dominant amyloid heart involvement and identification of a preferentially involved germline gene, IGLV1-44. *Blood* **119**, 144–150 (2012).
 7. Prokaeva, T. et al. Soft tissue, joint, and bone manifestations of AL amyloidosis: clinical presentation, molecular features, and survival. *Arthritis Rheum.* **56**, 3858–3868 (2007).
 8. Abraham, R. S. et al. Immunoglobulin light chain variable (V) region genes influence clinical presentation and outcome in light chain-associated amyloidosis (AL). *Blood* **101**, 3801–3807 (2003).
 9. Merlini, G. & Palladini, G. Light chain amyloidosis: the heart of the problem. *Haematologica* **98**, 1492–1495 (2013).
 10. Absmeier, R. M., Rottenaicher, G. J., Svilenov, H. L., Kazman, P. & Buchner, J. Antibodies gone bad – the molecular mechanism of light chain amyloidosis. *FEBS J.* **290**, 1398–1419 (2023).
 11. Oberti, L. et al. Concurrent structural and biophysical traits link with immunoglobulin light chains amyloid propensity. *Sci. Rep.* **7**, 16809 (2017).
 12. Bourne, P. C. et al. Three-dimensional structure of an immunoglobulin light-chain dimer with amyloidogenic properties. *Acta Crystallogr. D. Biol. Crystallogr.* **58**, 815–823 (2002).
 13. Schiffer, M., Girling, R. L., Ely, K. R. & Edmundson, A. B. Structure of a λ -type Bence-Jones protein at 3.5-Å resolution. *Biochemistry* **12**, 4620–4631 (1973).
 14. Graziani, M. S. & Merlini, G. Serum free light chain analysis in the diagnosis and management of multiple myeloma and related conditions. *Expert Rev. Mol. Diagn.* **14**, 55–66 (2014).
 15. Radamaker, L. et al. Cryo-EM reveals structural breaks in a patient-derived amyloid fibril from systemic AL amyloidosis. *Nat. Commun.* **12**, 875 (2021).
 16. Swuec, P. et al. Cryo-EM structure of cardiac amyloid fibrils from an immunoglobulin light chain AL amyloidosis patient. *Nat. Commun.* **10**, 1269 (2019).
 17. Radamaker, L. et al. Cryo-EM structure of a light chain-derived amyloid fibril from a patient with systemic AL amyloidosis. *Nat. Commun.* **10**, 1103 (2019).
 18. Radamaker, L. et al. Role of mutations and post-translational modifications in systemic AL amyloidosis studied by cryo-EM. *Nat. Commun.* **12**, 6434 (2021).
 19. Puri, S. et al. The cryo-EM STRUCTURE of renal amyloid fibril suggests structurally homogeneous multiorgan aggregation in AL amyloidosis. *J. Mol. Biol.* **435**, 168215 (2023).
 20. Shi, Y. et al. Structure-based classification of tauopathies. *Nature* **598**, 359–363 (2021).
 21. Yang, Y. et al. Cryo-EM structures of amyloid- β 42 filaments from human brains. *Science* **375**, 167–172 (2022).
 22. Kumar, S. et al. Assay to rapidly screen for immunoglobulin light chain glycosylation: a potential path to earlier AL diagnosis for a subset of patients. *Leukemia* **33**, 254–257 (2019).
 23. Mellors, P. W. et al. MASS-FIX for the detection of monoclonal proteins and light chain N-glycosylation in routine clinical practice: a cross-sectional study of 6315 patients. *Blood. Cancer J.* **11**, 50 (2021).
 24. Nevone, A. et al. An N-glycosylation hotspot in immunoglobulin κ light chains is associated with AL amyloidosis. *Leukemia* **36**, 2076–2085 (2022).
 25. Kourelis, T. et al. MASS-FIX may allow identification of patients at risk for light chain amyloidosis before the onset of symptoms. *Am. J. Hematol.* **93**, E368–E370 (2018).
 26. Buxbaum, J. N. et al. Amyloid nomenclature 2022: update, novel proteins, and recommendations by the International Society of Amyloidosis (ISA) Nomenclature Committee. *Amyloid* **29**, 213–219 (2022).
 27. Gottwald, J. & Röcken, C. The amyloid proteome: a systematic review and proposal of a protein classification system. *Crit. Rev. Biochem. Mol. Biol.* **56**, 526–542 (2021).
 28. Lavatelli, F. et al. Mass spectrometry characterization of light chain fragmentation sites in cardiac AL amyloidosis: insights into the timing of proteolysis. *J. Biol. Chem.* **295**, 16572–16584 (2020).
 29. Lavatelli, F. et al. Amyloidogenic and associated proteins in systemic amyloidosis proteome of adipose tissue. *Mol. Cell. Proteom. MCP* **7**, 1570–1583 (2008).
 30. Vrana, J. A. et al. Classification of amyloidosis by laser microdissection and mass spectrometry-based proteomic analysis in clinical biopsy specimens. *Blood* **114**, 4957–4959 (2009).
 31. Rømer, A. M. A., Thorseth, M.-L. & Madsen, D. H. Immune modulatory properties of collagen in cancer. *Front. Immunol.* **12**, 791453 (2021).
 32. Bonnans, C., Chou, J. & Werb, Z. Remodelling the extracellular matrix in development and disease. *Nat. Rev. Mol. Cell Biol.* **15**, 786–801 (2014).
 33. Hynes, R. O. The extracellular matrix: not just pretty fibrils. *Science* **326**, 1216–1219 (2009).
 34. Richey, T. et al. Macrophage-mediated phagocytosis and dissolution of amyloid-like fibrils in mice, monitored by optical imaging. *Am. J. Pathol.* **189**, 989–998 (2019).
 35. Jackson, J. W. et al. Collagen inhibits phagocytosis of amyloid in vitro and in vivo and may act as a ‘don’t eat me’ signal. *Amyloid* **0**, 1–12 (2022).
 36. Giorgetti, S. et al. β 2-Microglobulin isoforms display an heterogeneous affinity for type I collagen. *Protein Sci.* **14**, 696–702 (2005).
 37. Homma, N., Gejyo, F., Isemura, M. & Arakawa, M. Collagen-binding affinity of beta-2-microglobulin, a preprotein of hemodialysis-associated amyloidosis. *Nephron* **53**, 37–40 (1989).
 38. Hoop, C. L. et al. Collagen I Weakly Interacts with the β -Sheets of β 2-Microglobulin and Enhances Conformational Exchange To Induce Amyloid Formation. *J. Am. Chem. Soc.* **142**, 1321–1331 (2020).
 39. Relini, A. et al. Collagen plays an active role in the aggregation of β 2-microglobulin under physiopathological conditions of dialysis-related amyloidosis*. *J. Biol. Chem.* **281**, 16521–16529 (2006).
 40. Harris, D. L., King, E., Ramsland, P. A. & Edmundson, A. B. Binding of nascent collagen by amyloidogenic light chains and amyloid fibrillogenesis in monolayers of human fibrocytes. *J. Mol. Recognit.* **13**, 198–212 (2000).
 41. Kalaria, R. N. & Pax, A. B. Increased collagen content of cerebral microvessels in Alzheimer’s disease. *Brain Res* **705**, 349–352 (1995).
 42. Shi, C., Gottschalk, W. K., Colton, C. A., Mukherjee, S. & Lutz, M. W. Alzheimer’s disease protein relevance analysis using human and mouse model proteomics data. *Front. Syst. Biol.* **3**, 1085577 (2023).
 43. Cheng, J. S. et al. Collagen VI protects neurons against A β toxicity. *Nat. Neurosci.* **12**, 119–121 (2009).
 44. Mazzini, G. et al. Protease-sensitive regions in amyloid light chains: what a common pattern of fragmentation across organs suggests about aggregation. *FEBS J.* **289**, 494–506 (2022).
 45. Scheres, S. H. W. Amyloid structure determination in RELION-3.1. *Acta Crystallogr. Sect. Struct. Biol.* **76**, 94–101 (2020).
 46. He, S. & Scheres, S. H. W. Helical reconstruction in RELION. *J. Struct. Biol.* **198**, 163–176 (2017).
 47. Dispenzieri, A. et al. N-Glycosylation of monoclonal light chains on routine MASS-FIX testing is a risk factor for MGUS progression. *Leukemia* **34**, 2749–2753 (2020).
 48. Rottenaicher, G. J., Absmeier, R. M., Meier, L., Zacharias, M. & Buchner, J. A constant domain mutation in a patient-derived antibody light chain reveals principles of AL amyloidosis. *Commun. Biol.* **6**, 1–11 (2023).

49. Morgan, G. J. & Kelly, J. W. The kinetic stability of a full-length antibody light chain dimer determines whether endoproteolysis can release amyloidogenic variable domains. *J. Mol. Biol.* **428**, 4280–4297 (2016).
50. Engvall, E., Hessel, H. & Klier, G. Molecular assembly, secretion, and matrix deposition of type VI collagen. *J. Cell Biol.* **102**, 703–710 (1986).
51. Furthmayr, H., Wiedemann, H., Timpl, R., Odermatt, E. & Engel, J. Electron-microscopical approach to a structural model of intima collagen. *Biochem. J.* **211**, 303–311 (1983).
52. Godwin, A. R. F., Starborg, T., Sherratt, M. J., Roseman, A. M. & Baldock, C. Defining the hierarchical organisation of collagen VI microfibrils at nanometre to micrometre length scales. *Acta Biomater.* **52**, 21–32 (2017).
53. Knupp, C. & Squire, J. M. A new twist in the collagen story—the type VI segmented supercoil. *EMBO J.* **20**, 372–376 (2001).
54. Baldock, C., Sherratt, M. J., Shuttleworth, C. A. & Kiely, C. M. The supramolecular organization of collagen VI microfibrils. *J. Mol. Biol.* **330**, 297–307 (2003).
55. Mouw, J. K., Ou, G. & Weaver, V. M. Extracellular matrix assembly: a multiscale deconstruction. *Nat. Rev. Mol. Cell Biol.* **15**, 771–785 (2014).
56. Beecher, N. et al. Collagen VI, conformation of α -domain arrays and microfibril architecture. *J. Biol. Chem.* **286**, 40266–40275 (2011).
57. Engel, J. et al. Structure and macromolecular organization of type VI collagen. *Ann. N. Y. Acad. Sci.* **460**, 25–37 (1985).
58. Endicott, J., Holden, P. & Fitzgerald, J. Authentication of collagen VI antibodies. *BMC Res. Notes* **10**, 358 (2017).
59. Morrow, S. M., Bissette, A. J. & Fletcher, S. P. Transmission of chirality through space and across length scales. *Nat. Nanotechnol.* **12**, 410–419 (2017).
60. Bäcklund, G. et al. Conducting microhelices from self-assembly of protein fibrils. *Soft Matter* **13**, 4412–4417 (2017).
61. McDermott, M. L., Vanselous, H., Corcelli, S. A. & Petersen, P. B. DNA's chiral spine of hydration. *ACS Cent. Sci.* **3**, 708–714 (2017).
62. Kawauchi, T. et al. Encapsulation of fullerenes in a helical PMMA cavity leading to a robust processable complex with a macromolecular helicity memory. *Angew. Chem. Int. Ed.* **47**, 515–519 (2008).
63. Thomas, A. R. et al. Protein fibril assisted chiral assembly of gold nanorods. *J. Mater. Chem. B* **10**, 6360–6371 (2022).
64. Mankar, S., Anoop, A., Sen, S. & Maji, S. K. Nanomaterials: amyloids reflect their brighter side. *Nano Rev.* **2**, <https://doi.org/10.3402/nano.v2i0.6032> (2011).
65. Misumi, Y. et al. Interaction between amyloid fibril formation and extracellular matrix in the proceedings of VIIIth International Symposium on Familial Amyloidotic Polyneuropathy. *Amyloid* **19**, 8–10 (2012).
66. Koike, H. & Katsuno, M. Transthyretin amyloidosis: update on the clinical spectrum, pathogenesis, and disease-modifying therapies. *Neurol. Ther.* **9**, 317–333 (2020).
67. Simpson, L. W., Szeto, G. L., Boukari, H., Good, T. A. & Leach, J. B. Collagen hydrogel confinement of Amyloid- β (A β) accelerates aggregation and reduces cytotoxic effects. *Acta Biomater.* **112**, 164–173 (2020).
68. Fernández de Larrea, C. et al. A practical approach to the diagnosis of systemic amyloidoses. *Blood* **125**, 2239–2244 (2015).
69. Gertz, M. A. et al. Definition of organ involvement and treatment response in immunoglobulin light chain amyloidosis (AL): A consensus opinion from the 10th International Symposium on Amyloid and Amyloidosis. *Am. J. Hematol.* **79**, 319–328 (2005).
70. Perfetti, V. et al. Inverse polymerase chain reaction for cloning complete human immunoglobulin variable regions and leaders conserving the original sequence. *Anal. Biochem.* **239**, 107–109 (1996).
71. Rohou, A. & Grigorieff, N. CTFIND4: fast and accurate defocus estimation from electron micrographs. *J. Struct. Biol.* **192**, 216–221 (2015).
72. Zheng, S. Q. et al. MotionCor2: anisotropic correction of beam-induced motion for improved cryo-electron microscopy. *Nat. Methods* **14**, 331–332 (2017).
73. Emsley, P. & Cowtan, K. Coot: model-building tools for molecular graphics. *Acta Crystallogr. D. Biol. Crystallogr.* **60**, 2126–2132 (2004).
74. Croll, T. I. ISOLDE: a physically realistic environment for model building into low-resolution electron-density maps. *Acta Crystallogr. Sect. Struct. Biol.* **74**, 519–530 (2018).
75. Pettersen, E. F. et al. UCSF ChimeraX: Structure visualization for researchers, educators, and developers. *Protein Sci. Publ. Protein Soc.* **30**, 70–82 (2021).
76. Afonine, P. V. et al. Real-space refinement in PHENIX for cryo-EM and crystallography. *Acta Crystallogr. Sect. Struct. Biol.* **74**, 531–544 (2018).
77. Reily, C., Stewart, T. J., Renfrow, M. B. & Novak, J. Glycosylation in health and disease. *Nat. Rev. Nephrol.* **15**, 346–366 (2019).
78. Lawson, C. L. et al. EMDatabank unified data resource for 3DEM. *Nucleic Acids Res* **44**, D396–D403 (2016).
79. Davis, I. W. et al. MolProbity: all-atom contacts and structure validation for proteins and nucleic acids. *Nucleic Acids Res* **35**, W375–W383 (2007).
80. Punjani, A., Rubinstein, J. L., Fleet, D. J. & Brubaker, M. A. cryoSPARC: algorithms for rapid unsupervised cryo-EM structure determination. *Nat. Methods* **14**, 290–296 (2017).
81. Berisio, R., Vitagliano, L., Mazzarella, L. & Zagari, A. Crystal structure of the collagen triple helix model [(Pro-Pro-Gly)₁₀]₃. *Protein Sci. Publ. Protein Soc.* **11**, 262–270 (2002).
82. Mastronarde, D. N. Automated electron microscope tomography using robust prediction of specimen movements. *J. Struct. Biol.* **152**, 36–51 (2005).
83. Eisenstein, F. et al. Parallel cryo electron tomography on in situ lamellae. *Nat. Methods* **20**, 131–138 (2023).
84. Kremer, J. R., Mastronarde, D. N. & McIntosh, J. R. Computer visualization of three-dimensional image data using IMOD. *J. Struct. Biol.* **116**, 71–76 (1996).
85. Liu, Y.-T. et al. Isotropic reconstruction for electron tomography with deep learning. *Nat. Commun.* **13**, 6482 (2022).
86. Frank, J. et al. SPIDER and WEB: processing and visualization of images in 3D electron microscopy and related fields. *J. Struct. Biol.* **116**, 190–199 (1996).
87. Wickham, H. *Ggplot2: Elegant Graphics for Data Analysis*. (Springer International Publishing, New York, NY, 2016).
88. Wickham, H. et al. Welcome to the Tidyverse. *J. Open Source Softw.* **4**, 1686 (2019).
89. R Core Team. R: A language and environment for statistical computing. R Foundation for Statistical Computing (2020).
90. Li, Z., Jaroszewski, L., Iyer, M., Sedova, M. & Godzik, A. FATCAT 2.0: towards a better understanding of the structural diversity of proteins. *Nucleic Acids Res* **48**, W60–W64 (2020).
91. The UniProt Consortium. UniProt: the universal protein knowledgebase in 2021. *Nucleic Acids Res* **49**, D480–D489 (2021).
92. Gouet, P., Courcelle, E., Stuart, D. I. & Métois, F. ESPript: analysis of multiple sequence alignments in PostScript. *Bioinforma. Oxf. Engl.* **15**, 305–308 (1999).
93. Madden, T. L., Tatusov, R. L. & Zhang, J. Applications of network BLAST server. *Methods Enzymol.* **266**, 131–141 (1996).
94. Chenna, R. et al. Multiple sequence alignment with the Clustal series of programs. *Nucleic Acids Res* **31**, 3497–3500 (2003).
95. Perez-Riverol, Y. et al. The PRIDE database resources in 2022: a hub for mass spectrometry-based proteomics evidences. *Nucleic Acids Res* **50**, D543–D552 (2022).

Acknowledgements

This study was partially supported by Ricerca Corrente funding from Italian Ministry of Health to IRCCS Policlinico San Donato; Centro di Ricerca Pediatrica, Fondazione Romeo and Enrica Invernizzi (Milan, Italy); Italian Ministry of Research PRIN 2020 (20207XLJB2); CARIPLO/TELETHON Foundations (GJC23044); Deutsche Forschungsgemeinschaft (DFG, German Research Foundation) under Germany's Excellence Strategy (EXC 2067/1-390729940) and Italian Ministry of Health (RF-2016-02361756). Cryo-ET instrumentation was jointly funded by the DFG Major Research Instrumentation program (448415290) and the Ministry of Science and Culture of the State of Lower Saxony. K.S. and R.F.-B. were funded by the joint efforts of The Michael J. Fox Foundation for Parkinson's Research (MJFF) and the Aligning Science Across Parkinson's (ASAP) initiative. MJFF administers the grant ASAP-000282 on behalf of ASAP and itself. We are grateful to T. Cheng for assistance in cryo-ET experiments and T. Shaikh for advice on cryo-ET data processing.

Author contributions

Conceptualisation and Supervision by R.F.B., G.P., A.C.S., and S.R. Investigation and Analysis by T.S., A.C.S., V.S., K.S., G.Maz., S.C., C.M., P.R., A.C., P.F., and P.M. Funding acquisition and Resources by G.Mer., G.P., L.A., C.P., R.F.B., M.B., and S.R. Original draft by T.S., V.S., G.Maz., K.S., and A.C. Review and Editing by G.Mer., M.B., M.N., G.P., R.F.B., L.D., and S.R. Data visualisation by T.S., K.S., G.Maz., and A.C., edited and reviewed by T.S. and S.R. Contribution to and approval of the submitted version by all authors.

Competing interests

The authors declare no competing interests.

Additional information

Supplementary information The online version contains supplementary material available at <https://doi.org/10.1038/s41467-024-50686-2>.

Correspondence and requests for materials should be addressed to Stefano Ricagno.

Peer review information *Nature Communications* thanks Sjors Scheres, Luis Yauner and the other, anonymous, reviewer(s) for their contribution to the peer review of this work. A peer review file is available.

Reprints and permissions information is available at <http://www.nature.com/reprints>

Publisher's note Springer Nature remains neutral with regard to jurisdictional claims in published maps and institutional affiliations.

Open Access This article is licensed under a Creative Commons Attribution-NonCommercial-NoDerivatives 4.0 International License, which permits any non-commercial use, sharing, distribution and reproduction in any medium or format, as long as you give appropriate credit to the original author(s) and the source, provide a link to the Creative Commons licence, and indicate if you modified the licensed material. You do not have permission under this licence to share adapted material derived from this article or parts of it. The images or other third party material in this article are included in the article's Creative Commons licence, unless indicated otherwise in a credit line to the material. If material is not included in the article's Creative Commons licence and your intended use is not permitted by statutory regulation or exceeds the permitted use, you will need to obtain permission directly from the copyright holder. To view a copy of this licence, visit <http://creativecommons.org/licenses/by-nc-nd/4.0/>.

© The Author(s) 2024

¹Institute of Molecular and Translational Cardiology, IRCCS Policlinico San Donato, Piazza Malan 2, 20097 San Donato Milanese, Italy. ²Dept of Biochemistry and Biophysics, National Bioinformatics Infrastructure Sweden, Science for Life Laboratory, Stockholm University, Box 1031, SE-17121 Solna, Sweden. ³Department of Biosciences, Università degli Studi di Milano, Milan 20133, Italy. ⁴University Medical Center Göttingen, Institute for Neuropathology, Göttinge 37077, Germany. ⁵Aligning Science Across Parkinson's (ASAP) Collaborative Research Network, Chevy Chase, MD, USA. ⁶Amyloidosis Treatment and Research Center, Fondazione IRCCS Policlinico San Matteo, Università Degli Studi di Pavia, Pavia 27100, Italy. ⁷Department of Molecular Biochemistry and Pharmacology, Istituto di Ricerche Farmacologiche Mario Negri IRCCS, Via M. Negri 2, Milano 20156, Italy. ⁸Faculty of Medicine and Surgery, Vita-Salute San Raffaele University, Milan 20132, Italy. ⁹Arrhythmia and Electrophysiology Department, IRCCS Policlinico San Donato, San Donato, Milan 20097, Italy. ¹⁰Cluster of Excellence "Multiscale Bioimaging: from Molecular Machines to Networks of Excitable Cells" (MBExC), University of Göttingen, Göttingen 37077, Germany. ¹¹Faculty of Physics, University of Göttingen, Göttingen 37077, Germany. ¹²These authors contributed equally: Tim Schulte, Antonio Chaves-Sanjuan, Valentina Speranzini. ✉ e-mail: stefano.ricagno@unimi.it